Supporting Information

Effect of Quencher, Geometry, and Light Out-Coupling on the Determination of Exciton Diffusion Length in Nonfullerene Acceptors

Valentina Belova[1,†,], Aleksandr Perevedentsev[1,†], Julien Gorenflot[2,†,*], Catherine S. P. De Castro[2], Miquel Casademont-Viñas[1], Sri H. K. Paleti,[2] Safakath Karuthedath[2], Derya Baran[2], Frédéric Laquai[2], Mariano Campoy-Quiles[1,*]*

1 - Nanopto Group, Nanostructured Materials for Optoelectronics and Energy Harvesting Research Unit, Material Science Institute of Barcelona, ICMAB-CSIC, 08193 Bellaterra, Spain
2 - King Abdullah University of Science and Technology (KAUST), KAUST Solar Center (KSC), Physical Sciences and Engineering Division (PSE), Materials Science and Engineering Program (MSE), Thuwal 23955-6900, Kingdom of Saudi Arabia

**valentina.belova@esrf.fr*
**julien.gorenflot@kaust.edu.sa*
**mcampoy@icmab.es*

Table of contents

† Those authors contributed equally to this work

1. Comparison of the reported L_D

Table S1. Reported L_D [nm] values of OPV materials obtained by different methods

Material	photocurrent	PL surface quenching	spectrally-resolved PL surface quenching	TR PL volume quenching	exciton-exciton annihilation
C_{60}	14.1[1] 40±5[2] 30-35[3]				
PPV	12±3[4] 7±1[5]				
CuPc	68±20[4] 8±3[2]				
PTCDA	225±15 (CT), 88±6 (triplet)[6]		10.4±1.0[7] 9.3±0.8[8]		
SubPc		7.7[9] 10.7[10]	8.0±0.3[7] 15.5-22.7[8]		
DIP		60[11]	16.5±1.0 (up-right), 21.8±0.6 (flat)[7]		
TPA-T-DCV-Ph(F)		26[12]		16[13]	
ITIC	25[14]			18±2[15]	31.9±0.7[14]
IT-4F	45[14]			19±2[15]	47.4±0.9[14]
IDIC	24[14]				16-35[16]

2. Optical indices

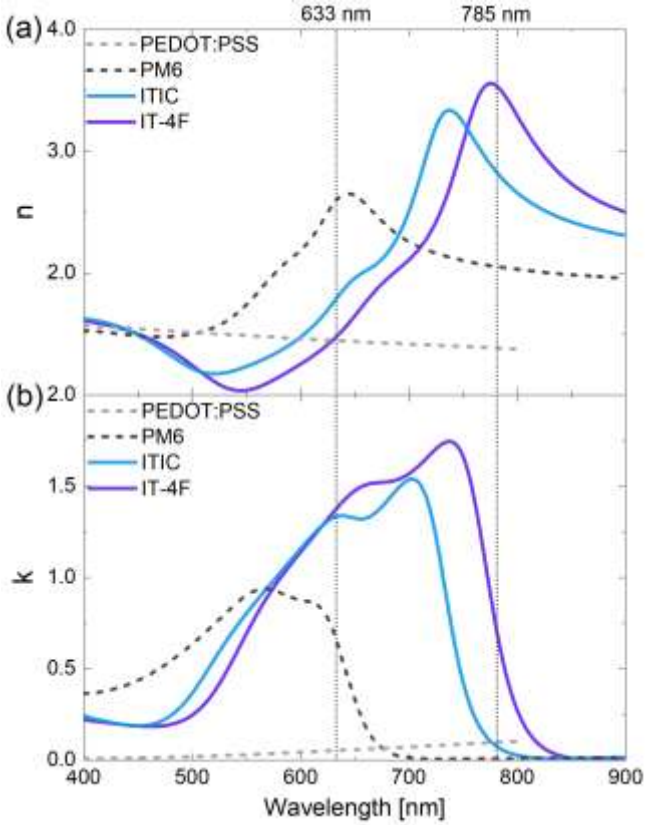

Figure S1. Optical indices n (a) and k (b) extracted by spectroscopic ellipsometry.

3. Photoelectron spectroscopy in air (PESA)

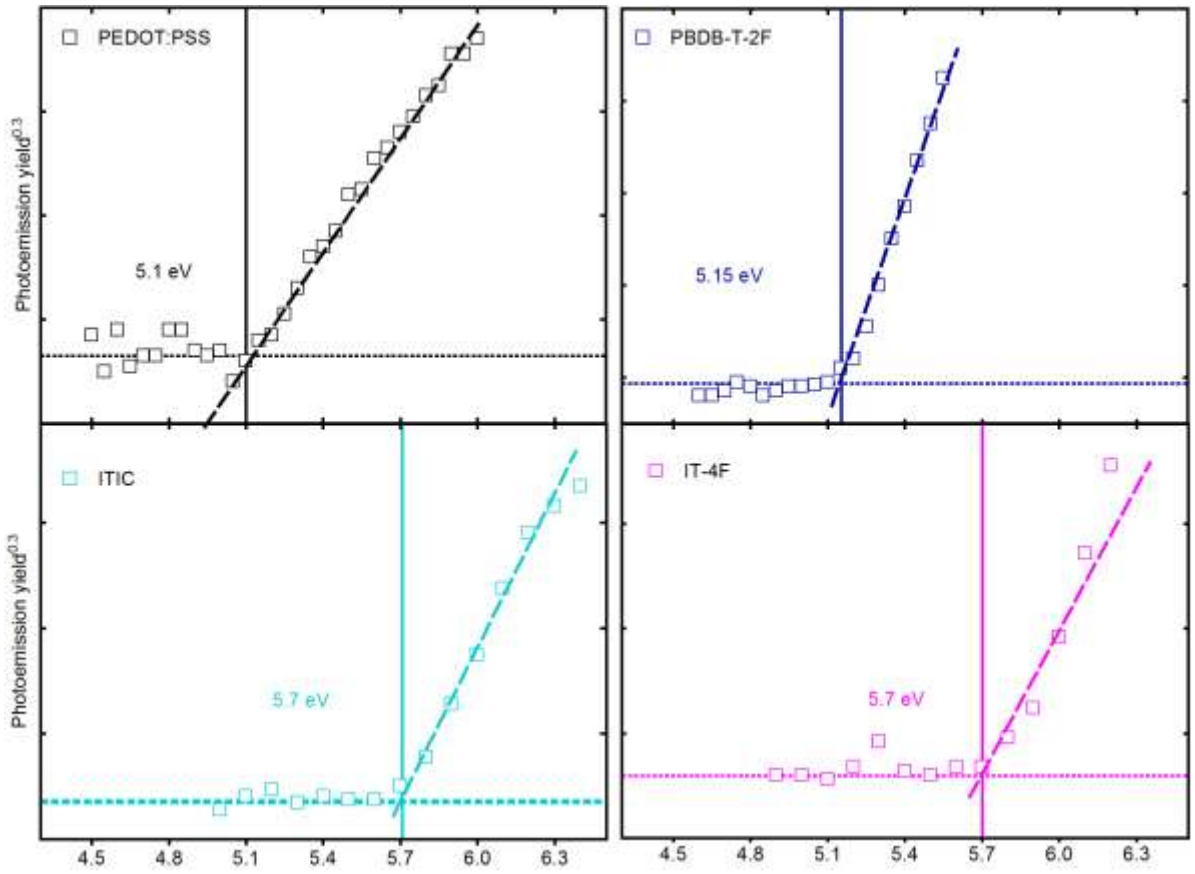

Figure S2. PESA data of two acceptors as well as the considered exciton quenchers. The estimated ionisation energies are denoted in the plots.

4. Floating method

The sequential processing steps shown in Figure S3 are:

(1) Deposition by blade-coating onto a glass substrate of an ITIC film featuring a thickness gradient along the coating direction, as enabled by a continuous variation of blade speed from fast (thicker film) to slow (thinner film).

(2) Deposition by blade-coating onto another glass substrate of a pNaSS film. A film thickness of ~10 nm enables optimal floating of any subsequently deposited polymer films.

(3) Deposition by blade-coating onto the pNaSS film of a PM6 film. Given the pNaSS is (almost) exclusively soluble in water offers a wide selection of solvents for film deposition in this step, thereby avoiding any inter-diffusion between these sequentially deposited films. A diamond scribe is used to define the film region for subsequent floating transfer and to create an undercut. The latter facilitates the release of the PM6 film in the following step which, otherwise, is prone to wrinkling or tearing due to its stronger adhesion to substrate at overlapping edges.

(4) The substrate coated with the pNaSS/PM6 films is slowly lowered into a petri dish with water. Dissolution of pNaSS releases the PM6 film to float on the water surface. Using a material with a molecular weight that enables a substantial entanglement density provides sufficient toughness to avoid break-up of the film during this step.

(5) The substrate coated with the ITIC film is rapidly lowered into the same petri dish, positioned parallel to the floating PM6 film, and slowly drawn up edge-first. After the edge of the PM6 film is hooked onto the ITIC film, subsequent draw-up is performed at a steeper angle to minimize the trapping of water between two films.

(6) The obtained ITIC/PM6 film is then desiccated to remove any residual water and form conformal contact between the two films.

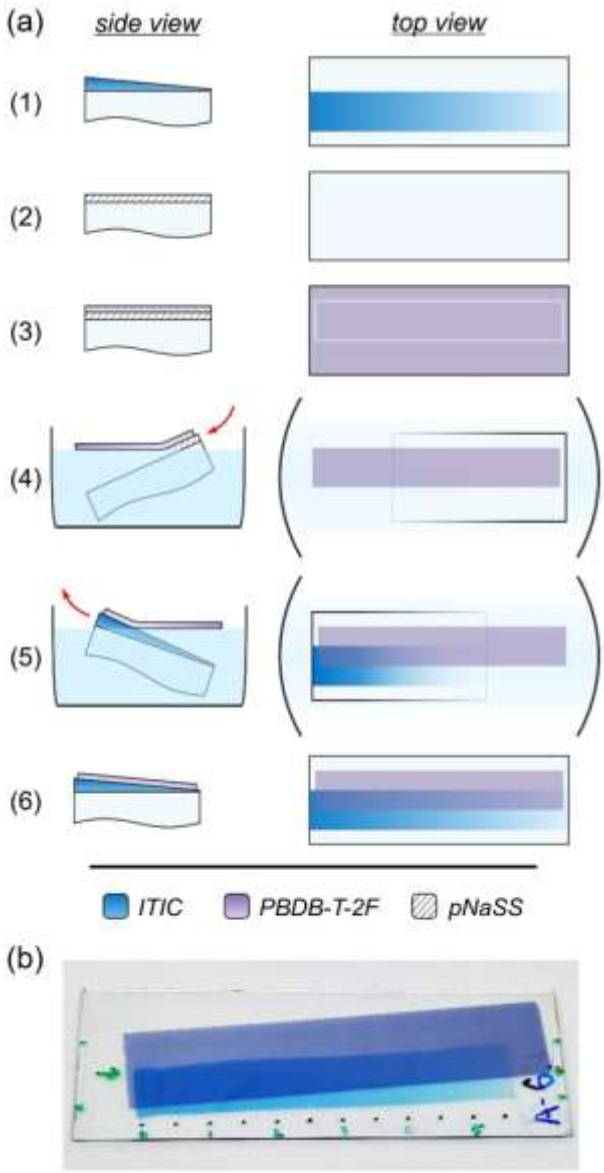

Figure S3. (a) Schematic illustration of the 'floating transfer' method employed for fabricating ITIC/PM6 bilayer films. (b) A bilayer sample prepared by the 'floating transfer' method.

5. Annealing test

Figure S4 shows quenching efficiency QE curves measured on a pristine ITIC/PM6 sample and after each of three thermal annealing steps: at 100 °C for 30 min, at 180 °C for 60 min, and at 220 °C for 50 min. Each annealing step was carried out in a nitrogen atmosphere on a ceramic hotplate.

As known from the literature, ITIC undergoes a sub-T_g relaxation at approximately 60-80 °C.[17] Above this temperature, it has limited but non-negligible mobility and can undergo diffusion-limited crystallisation. The second annealing temperature of 180 °C was chosen to match the reported T_g of ITIC.[17] There is no data on the T_g of PM6 available but one can assume it behaves similar to the related polymer PBDB-T which has a T_g with onset around 90-100 °C.[18] Thus annealing of ITIC/PM6 at 100 °C, therefore, would not lead to a major interdiffusion. However, if the contact between bilayer films is not perfectly conformal (e.g. due to frozen-in strain) then this annealing step would "heal it" because the films are mechanically softened at this temperature. The fact that there is no major difference seen between "pristine" and "100 °C" data indicates that the interface is already conformal in the pristine, as-prepared samples. Hence the difference in the QE behaviour between ITIC/PM6 and ITIC/PEDOT:PSS is not due to processing-related interface characteristics.

On the other hand, annealing at, or above, T_g is known to activate a significant interdiffusion and, in case of ITIC, polymorphic changes.[19] Therefore "180 °C" and "220 °C" data is consistent since the interdiffusion leads to an increase of the QE as expected.

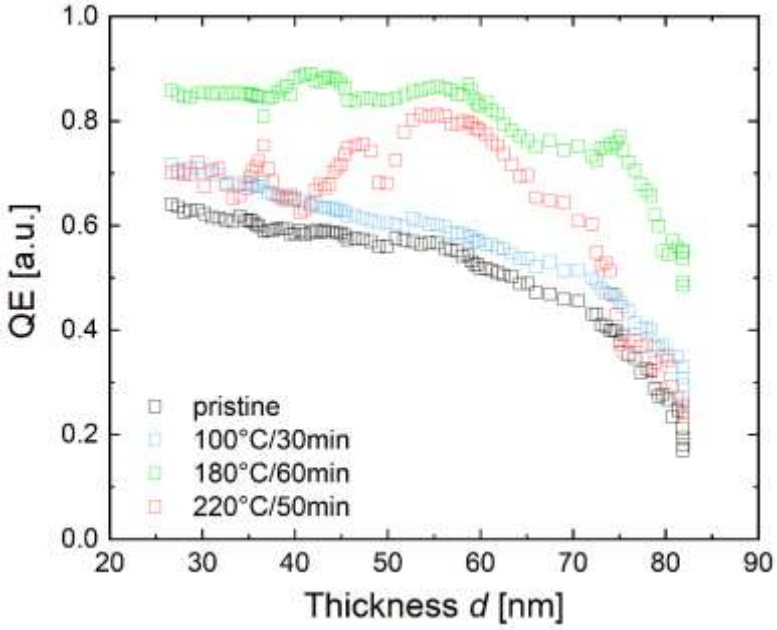

Figure S4. QE versus *d* curves measured on a pristine ITIC/PM6 sample and after several steps of thermal annealing.

6. Roughness

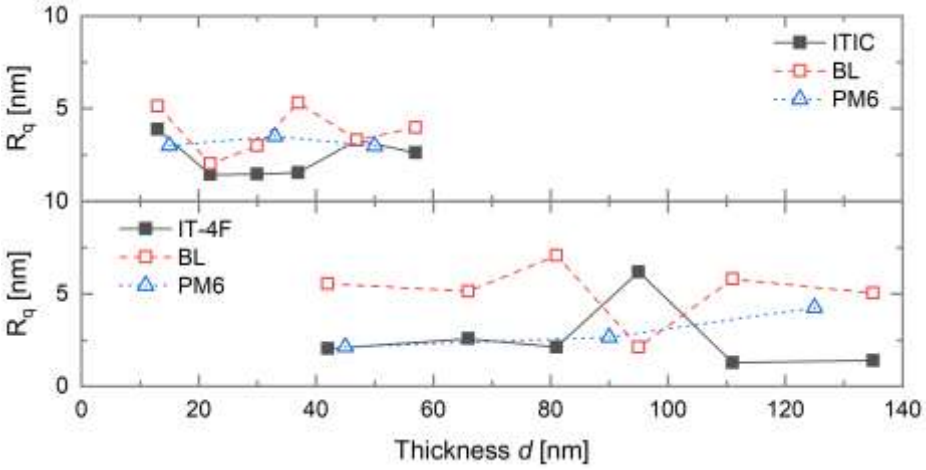

Figure S5. Measured profile roughness R_q of ITIC, IT-4F (black) in comparison with the R_q of the corresponding bilayer (BL, red) and PM6 single layers (blue) as a function of the NFA thickness *d*.

7. Outcoupling and apparent quenching simulation

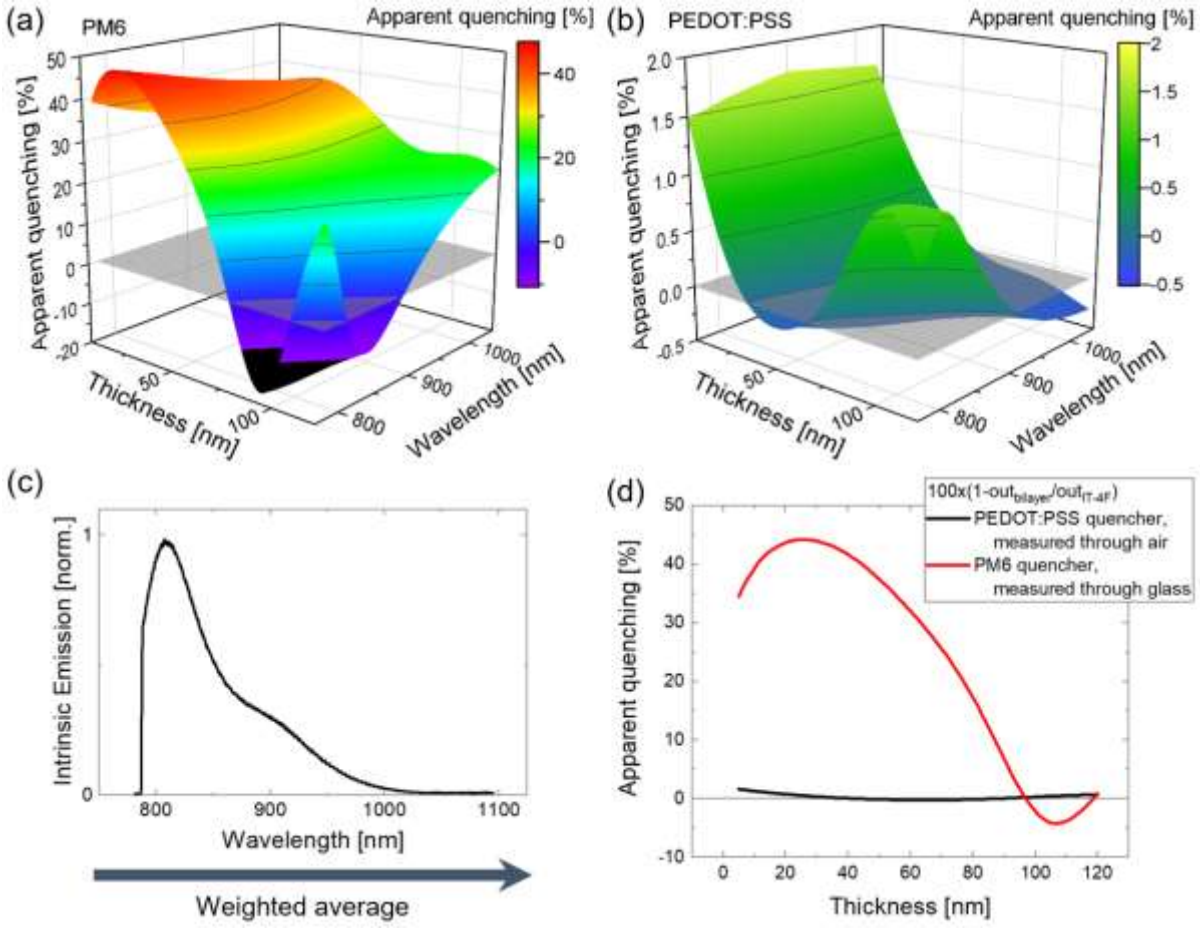

Figure S6. Apparent quenching computed as the value that $QE = 1 - \frac{PL_{BL}(d)}{PL_{emitter}(d)}$ would take in the absence of actual exciton quenching, that is considering only the difference of light absorption and out-coupling between the BL and the emitter alone. Here simulated for the case of IT-4F and for an excitation wavelength of 785 nm. (a-b) Spectral dependence considering a hypothetical intrinsically uniform emission (c) Intrinsic PL emission spectrum of the IT-4F film used to calculate the weighted average. This spectrum is obtained by correcting the emission spectra for the spectrally dependent outcoupling for different IT-4F thicknesses and averaging them (practically: averaging the spectra shown in Figure 6d). (d) Weighted average of the apparent quenching, using the intrinsic emission spectrum as a weight.

8. Evolution of the exciton lifetime probed by time resolved spectroscopy

We monitored the evolution of the exciton with transient absorption spectroscopy on an IT-4F sample, both in the IT-4F and the bilayer part. As can be seen in Figure S7b, even for the thinner IT-4F condition, no significant evolution of the spectral shape could be observed in

the bilayer, indicative of the presence of only on excited species: the primarily generated IT-4F exciton.[20]

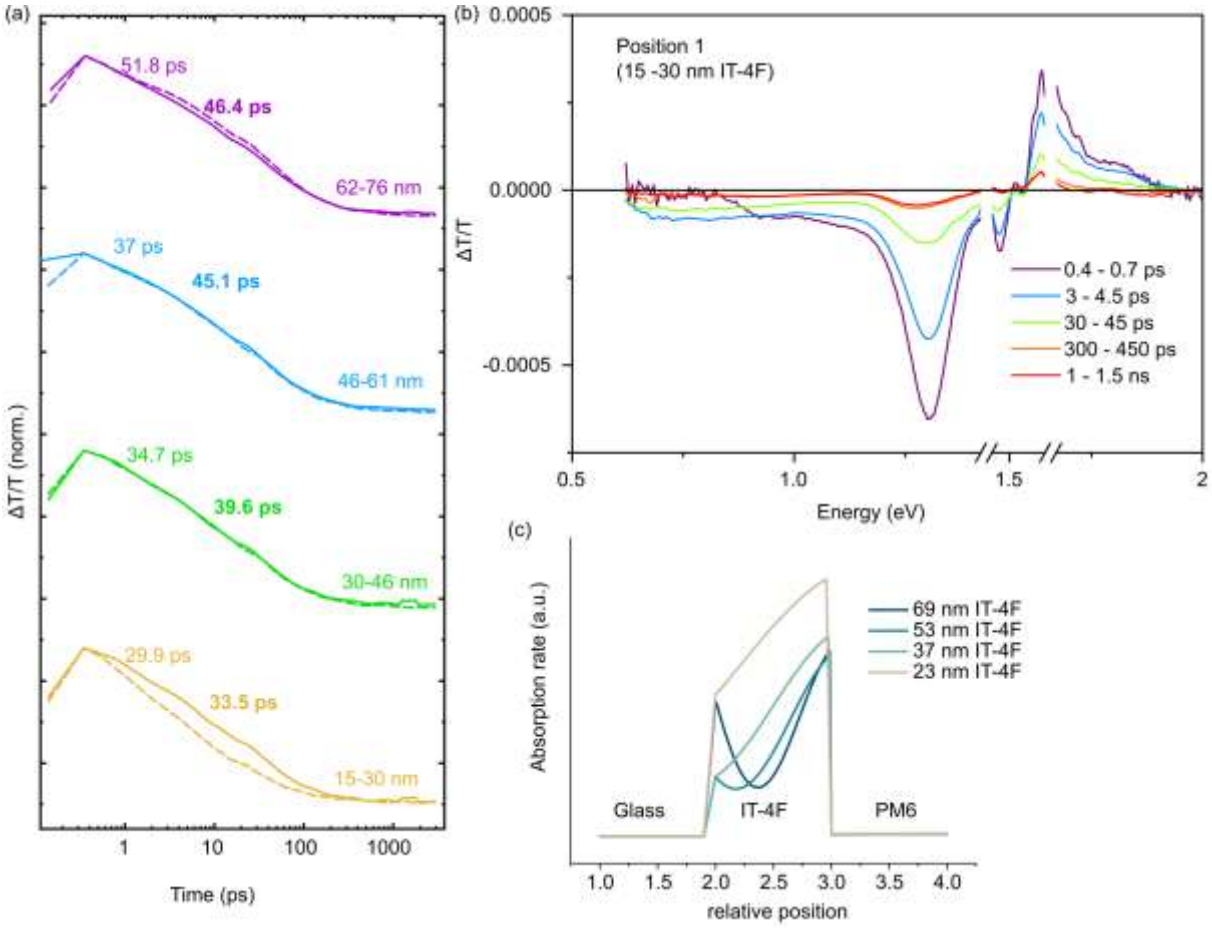

Figure S7. Transient evolution of the exciton signal following a pulsed excitation for an IT-4F sample excited at 750 nm. (a) Kinetics in the IT-4F (dashed lines) and bilayer (solid lines) for different positions through the gradient. (b) Spectra at different time delays measured on the bilayer, for a position corresponding to an IT-4F thickness between 15 and 30 nm. (c) Absorption profile through the IT-4F layer for the 4 investigated positions.

Moreover, the kinetics of the signal (Figure S7a) indicate no reduction of the exciton lifetime in the bilayers (solid lines) compared with the pristine IT-4F (dashed lines). It has to be stressed however, that the exciton lifetime seems to be influenced by the initial exciton density (see absorption profiles in Figure S7c), which is a strong indication that the decay is dominated by exciton-exciton annihilation. This also explains why the lifetimes are shorter that what is typically expected for excitons in organic semiconductors (we recently reported a value of 87 ps for IT-4F)[20]. One can thus expect that some interface quenching could

become detectable at lower fluences once the exciton lifetime becomes sufficient for them to reach the interface. Unfortunately, rather low fluences were already used (1 μJ/cm^2) and it was not possible to further reduce it while keeping a useful amount of signal.

A detailed description of the experiment can be found elsewhere.[14]

9. Absorption under 633 nm excitation

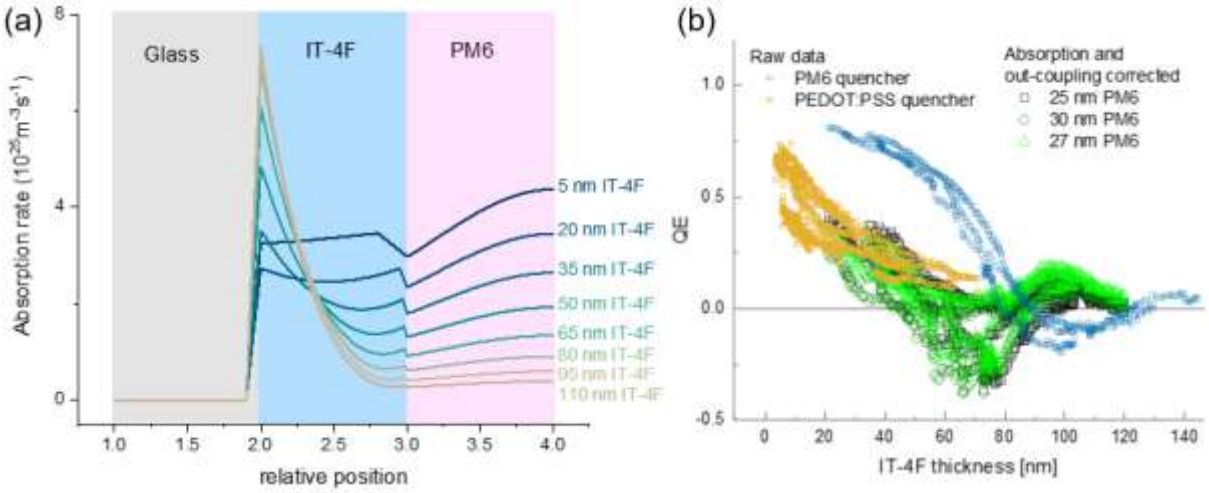

Figure S8. Optical correction under 633 nm excitation. (a) Absorption profile simulation in a glass/IT-4F/PM6 sample excited at 633 nm (light coming from the glass), for different IT-4F thicknesses. As can be seen even up to large IT-4F thicknesses, the light absorption in the PM6 layer remains considerable. (b) QE as measured and corrected for the light absorption and out-coupling: the corrected QE becomes negative around 40 nm, we attribute this to the additional excitation of the IT-4F layer due to energy transfer from the PM6, leading to a larger intrinsic emission in the bilayer than in the IT-4F alone. Correcting for the IT-4F absorption originating in the energy transfer from the PM6 side would require to know the PM6 exciton diffusion length and emission quantum yield as well as the forester energy transfer rate.

10. Separating absorption and out-coupling

Setfos can not specifically compute the out-coupling from a device as it is dependent on the absorption profile. As a reminder, the overall optical correction was computed by considering a given excitation and an intrinsically uniform emission, and simulating how much of this emission gets out of the sample as a function of the sample geometry and the layer thicknesses. This light getting out of the sample is thus a convolution of the quantity of light absorbed and the out-coupling efficiency.

However, because the absorption profile has to be included in the fit (as it controls how far an exciton has to diffuse to reach the quencher) the quenching efficiency should not be corrected for it, in order to extract the diffusion length. As a result, the influences of absorption and out-coupling have to be isolated.

To separate those two influences we integrated the simulated absorption profile (see Figure 4) to determine the quantity of light absorbed. Dividing the integrated simulated emitted light by this integrated absorbed light gives the out-coupling efficiency.

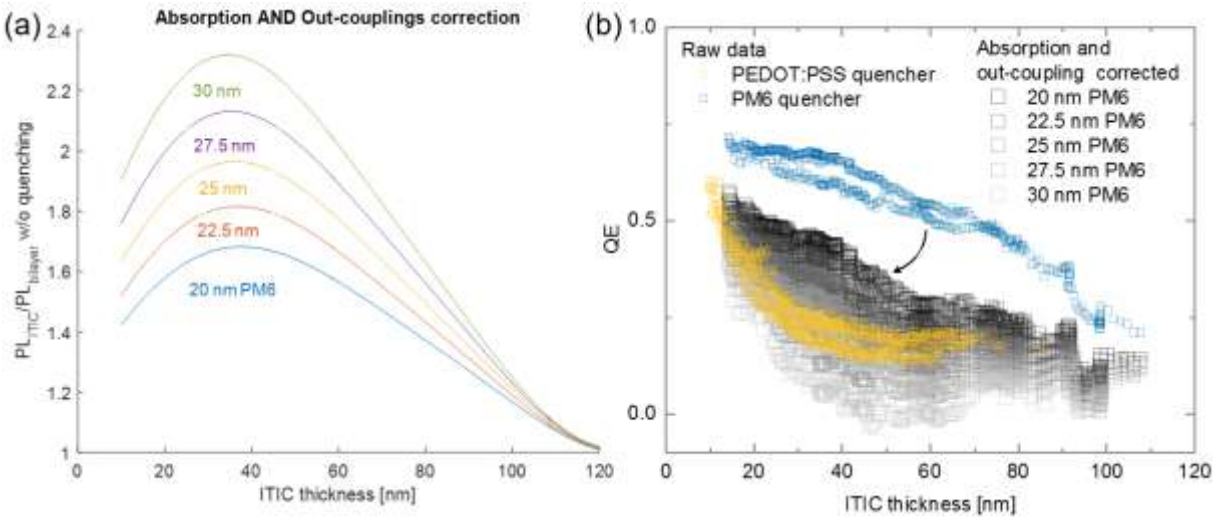

Figure S9. Applying the simulated absorption and outcoupling correction reveals the intrinsic quenching efficiency in the experiment using PM6 as quencher. Here in the case of ITIC. As can be seen, the correction is very sensitive to the quencher layer thickness that must thus be known with a very good precision. (a) QE correction factor, i.e. ratio of the simulated PL for emitter alone and bilayer, depending of the emitter thickness for different simulated PM6 layer thicknesses. (b) Measured and corrected QE.

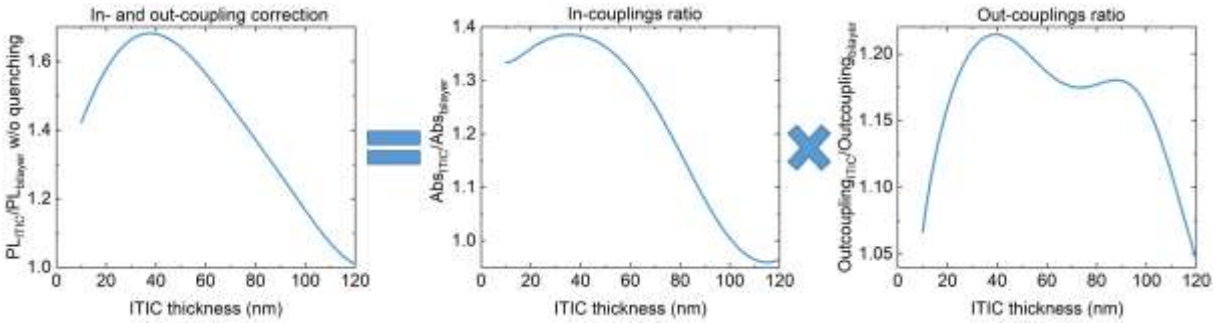

Figure S10. Decomposition of the correction into absorption and out-coupling corrections. Here is the case of ITIC with a 20 nm PM6 quencher.

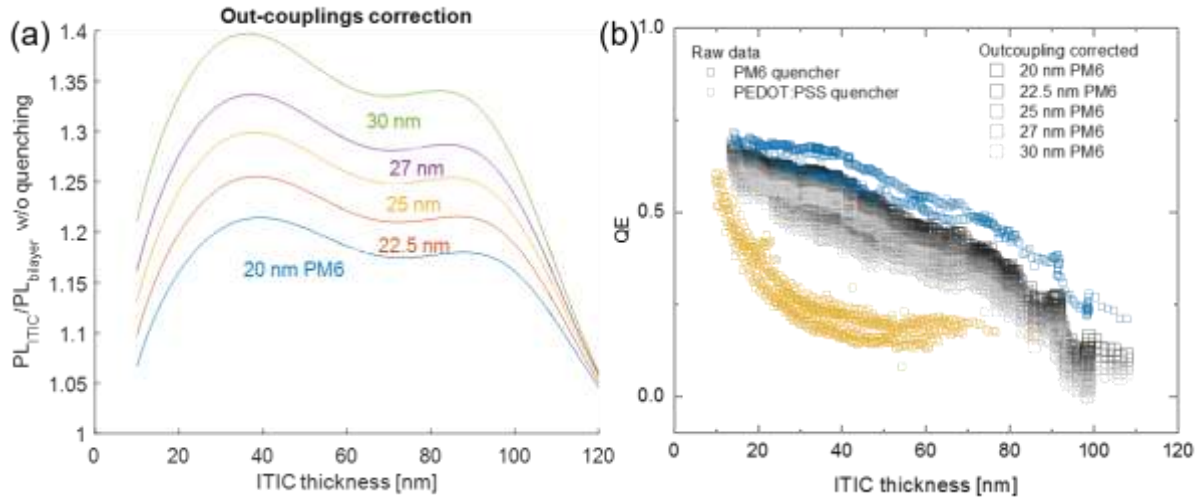

Figure S11. Applying only the out-coupling correction gives the thickness dependence of 1-$PL_{bilayer}/PL_{emitter}$ uncorrected for the difference in absorption, which is the variable that needs to be fitted to determine the exciton diffusion length. (a) Outcoupling correction factor. (b) Measured and corrected QE.

11. Complete (transfer matrix) versus simplified (Lambert-Beer law) exciton diffusion model

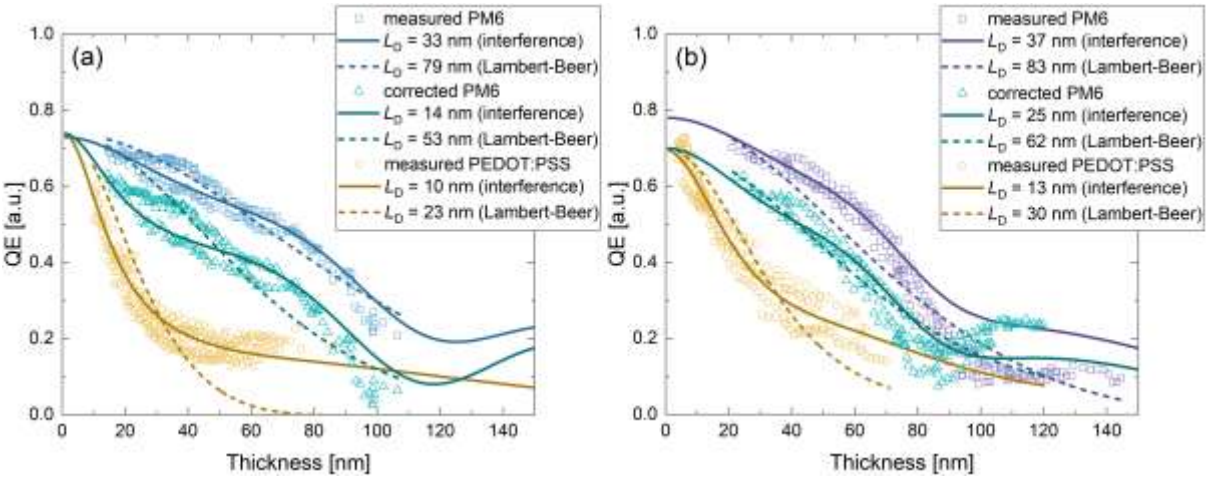

Figure S12. Comparison between the exciton diffusion model with the simplified exciton generation profile described by Lambert-Beer law and the more complete model with the estimated electric field interference for ITIC (a) and IT-4F (b) coupled with PM6 (measured and corrected QE curves) and PEDOT:PSS quenchers. 785 nm excitation.

12. Effect of quencher refractive index and thickness

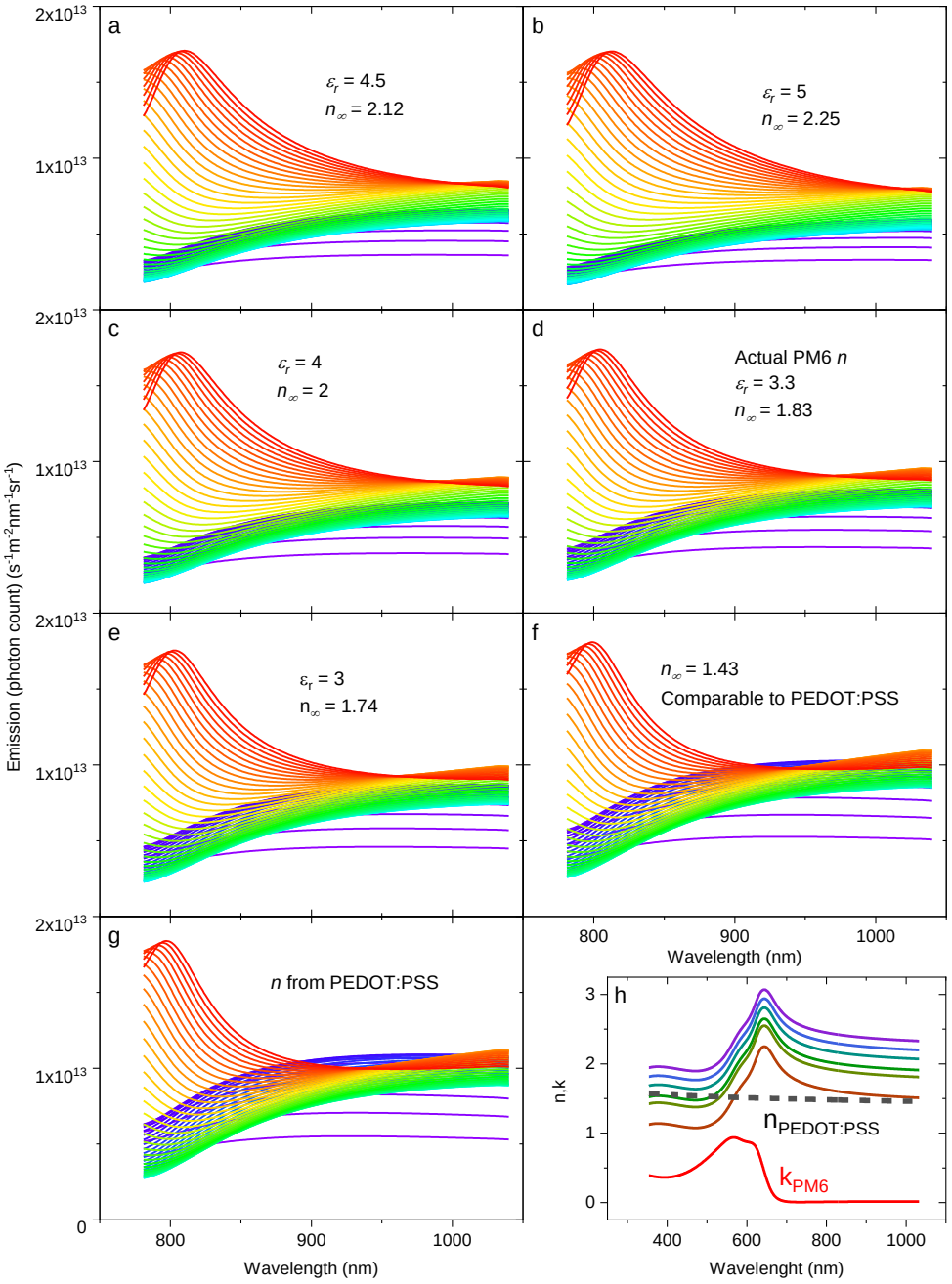

Figure S13. Output emission spectra simulated with the structure used for the IT-4F/PM6 bilayers excited at 780 nm but varying the optical indices of the quencher. (a-f) considering the same n spectra as n_{PM6} but shifted by a constant offset, corresponding to a typical value of organic semiconductor for (a-e), and shifted to have the same high wavelength index as PEDOT:PSS (f), for the simulation shown in (g), the actual refractive index of PEDOT:PSS was used. In all cases, the imaginary part k of the refractive index was kept the same as in PM6. (h) Summary of the refractive indexes used for the simulations.

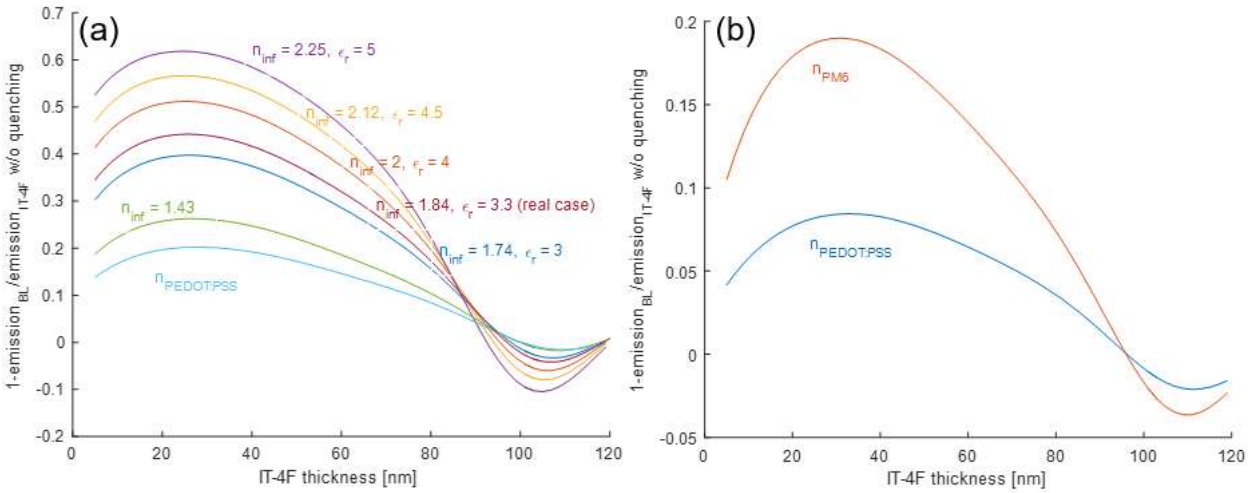

Figure S14. Evolution of the simulated apparent quenching for IT-4F excited at 785 nm for the quencher refractive indexes represented in Figure S13. (a) for a 25 nm thick quencher, (b) for a 10 nm thick quencher.

13. Effect of sample geometry

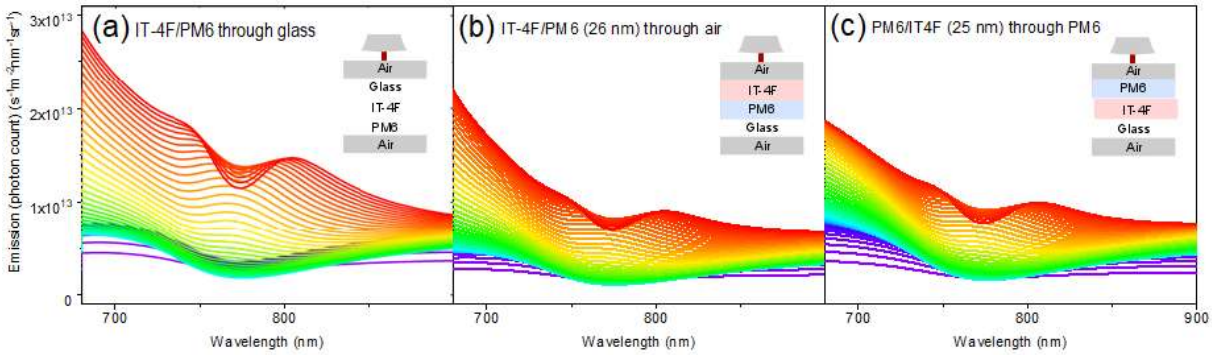

Figure S15. Output emission spectra simulated for different sample geometries with PM6 quencher: (a) emission through glass (actual experiment with the PM6 samples measured in the 'inverted' geometry from the bottom), (b) through air (as PEDOT:PSS samples), and (c) through PM6 (PM6 samples measured in the 'normal' geometry from the top).

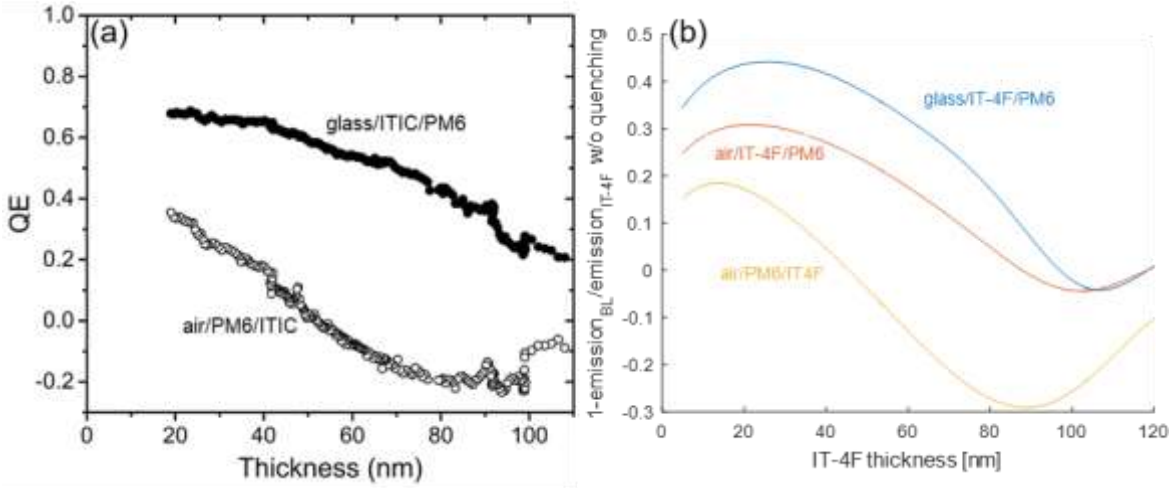

Figure S16. (a) Experimental QEs for the 'inverted' and 'normal' measurement geometries and (b) the calculated apparent quenching for the corresponding cases together with the 'through air' case.

14. Structurally modified ITIC layers

ITIC/PM6 bilayer samples were also prepared in which ITIC was crystallized by *solvent*-induced crystallization. In a number of (macro-)molecular materials, solvent-induced crystallization is known to enable the formation of crystalline microstructures that are inaccessible by thermal treatments, with well-known examples being those of syndiotactic polystyrene[21] and dialkyl-substituted polyfluorenes[22]. This aspect is especially relevant due to the exclusive use of solution-based processing in the field for depositing the studied materials. To this end, ITIC/PM6 bilayer samples were also prepared in which ITIC was crystallized with the aid of two different small-molecular 'solid solvents' – namely, biphenyl and lauric acid. While rarely employed in the field to-date, this approach was shown to be extremely versatile by the recent report on solid-solvent-assisted structuring of organic semiconductor films, in which both of the aforementioned solvents were employed.[23] Hereafter, the samples will be designated by a prefix indicative of the corresponding ITIC microstructure. ITIC samples crystallized using *biphenyl* and *lauric acid* 'solid solvents' will be designated as '*bp*-ITIC' and '*la*-ITIC' respectively.

Solvent-induced crystallization was performed by depositing overlayers of two small-molecular 'solid solvents' onto ITIC thickness gradients, followed by mild heating in ambient atmosphere. In the first case, biphenyl (melting temperature $T_m \approx 69$ °C) overlayers were spin-coated from 5 wt% solutions in acetonitrile (non-solvent of ITIC). Subsequent heating to 80 °C for 50 s led to dissolution of ITIC, followed by its recrystallization and, finally, complete evaporation of biphenyl. In the second care, lauric acid ($T_m \approx 44$ °C) overlayers were spin-coated from 2 wt% solutions in methanol (non-solvent of ITIC), followed by heating to 70 °C for 60 s to recrystallize ITIC and then 100 °C for a further 90 s to boil-off any residual lauric acid. Lamination of the obtained samples with PM6 was then performed as described above.

Both methods of crystallization employed induce unique drastic changes of the film absorption and PL spectra when compared to untreated ITIC samples (Figure S17, left): the pronounce red- and blue-shifts are seen for *bp*- and *la*-ITIC, respectively. This observation suggests that both treatments are polymorph-selective in their individual ways. Transmitted-light and cross-polarized microscopy images used to characterise the film homogeneity and microstructure, are shown in the right part of Figure S17. As-deposited ITIC is found to be, essentially, 'amorphous' (that is, no detectable in-plane order) as evidenced by the lack of birefringence in cross-polarized images. Similar observations are made for IT-4F samples (Figure S21). Solvent-crystallized ITIC films reveal the expected signature of birefringence in cross-polarized micrographs. A homogeneous fine-grained crystalline microstructure is observed for both *bp*- and *la*-ITICs. We note, that a detailed investigation of the formation and structure of solvent-induced ITIC polymorphs is beyond the scope of the present study and will be reported elsewhere.

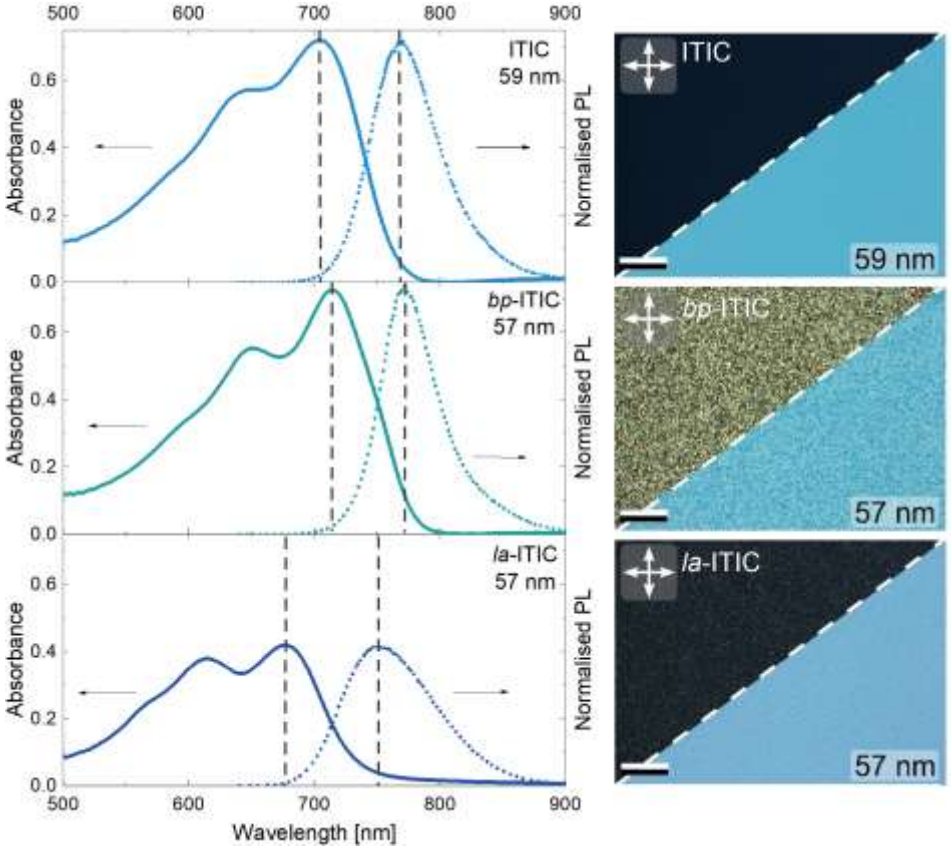

Figure S17. *Left*: Optical absorption and PL spectra of as-deposited ITIC and modified *bp*-ITIC and *la*-ITIC films of the indicated thickness. In each case, the vertical markers (dashed grey lines) indicate the spectral positions of the main peak. *Right*: Optical micrographs for the studied ITIC layers recorded at the indicated film thickness. Both cross-polarized (top-left panels) and transmitted-light (bottom-right panels) micrographs are shown. Scale bar = 50 μm.

The experimental (measured at 785 nm excitation) and out-coupling corrected QE data for solvent-modified ITIC gradients combined with PM6 quencher along with the corresponding modelled curves are provided in Figure S18. The fitting of the measured QE data leads to the L_D values around 30 nm for *bp*-ITIC and 45 nm for *la*-ITIC. After correcting for the light out-coupling, the resulting L_D decreases by more than a factor of two to 10-15 nm for *bp*-ITIC and 12-20 nm for *la*-ITIC. The corrected values are comparable with those obtained for as-deposited ITIC.

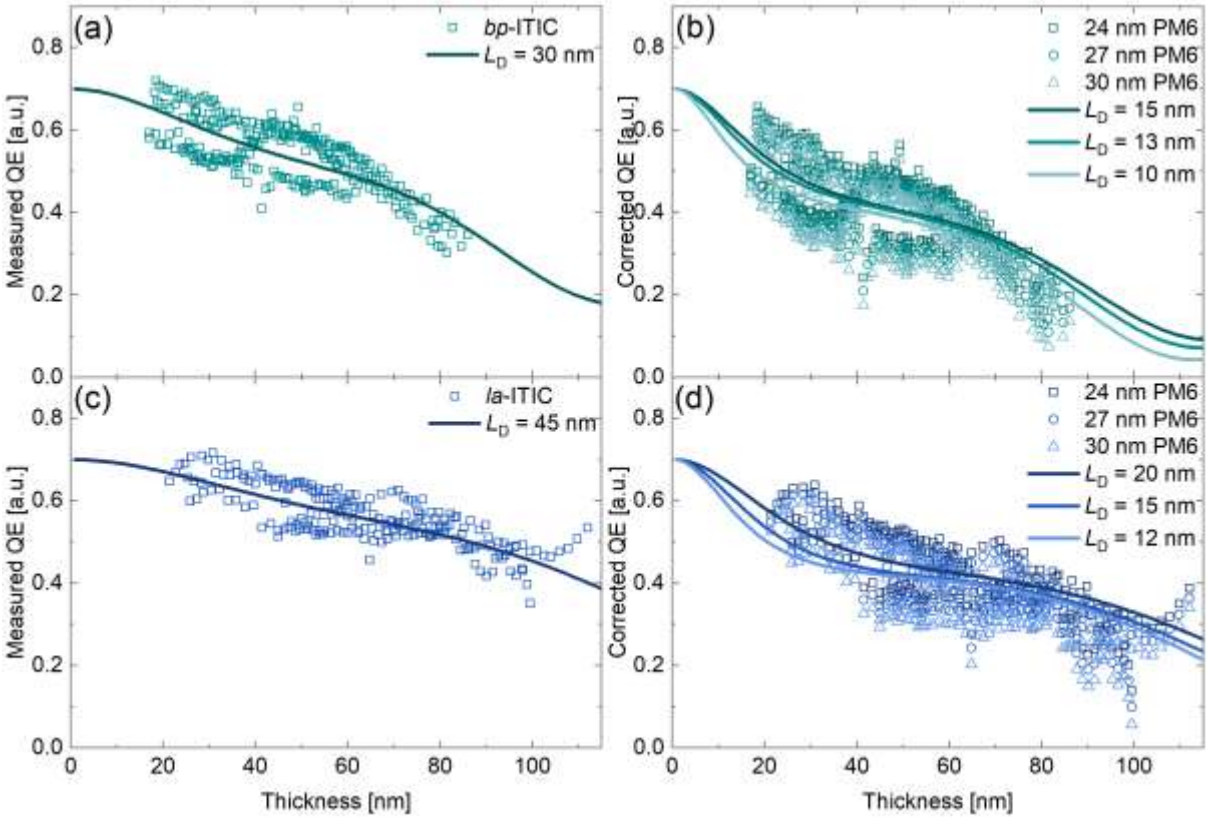

Figure S18. Measured (*left*) and corrected for out-coupling (*right*) QE data points of modified *bp*-ITIC/PM6 (a,b) and *la*-ITIC/PM6 (c,d) together with the corresponding modelled QE curves (solid lines). For the out-coupling correction, three different thicknesses of PM6 quencher are considered. The excitation wavelength is 785 nm. Only every third data point is shown for clarity.

15. Gradient thickness profiles and microscopy

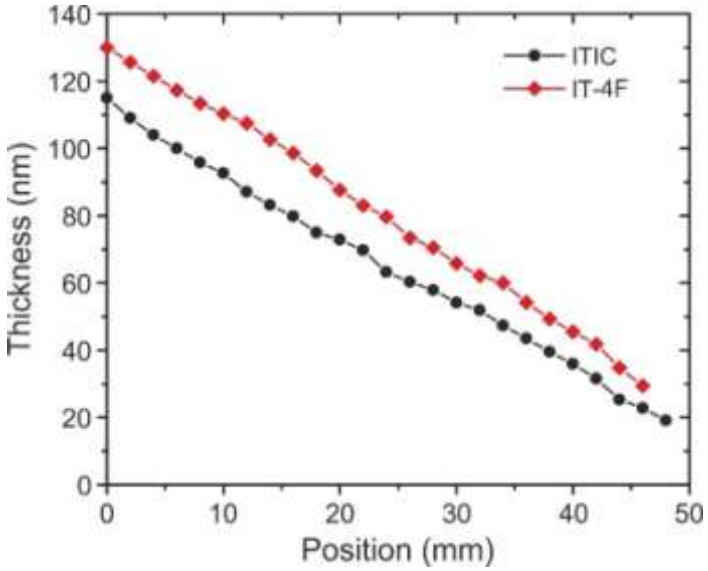

Figure S19. Representative thickness profiles of ITIC and IT-4F films deposited by variable-speed blade-coating. Data are plotted as a function of position along the coating direction (i.e. decreasing blade speed). Spectroscopic ellipsometry was applied to obtain the thickness values.

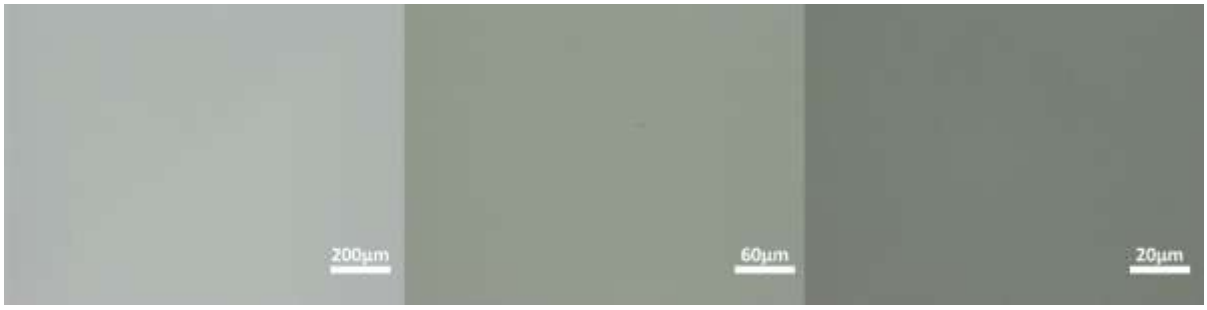

Figure S20. Transmitted-light micrographs for ITIC gradients film deposited on PEDOT:PSS layer.

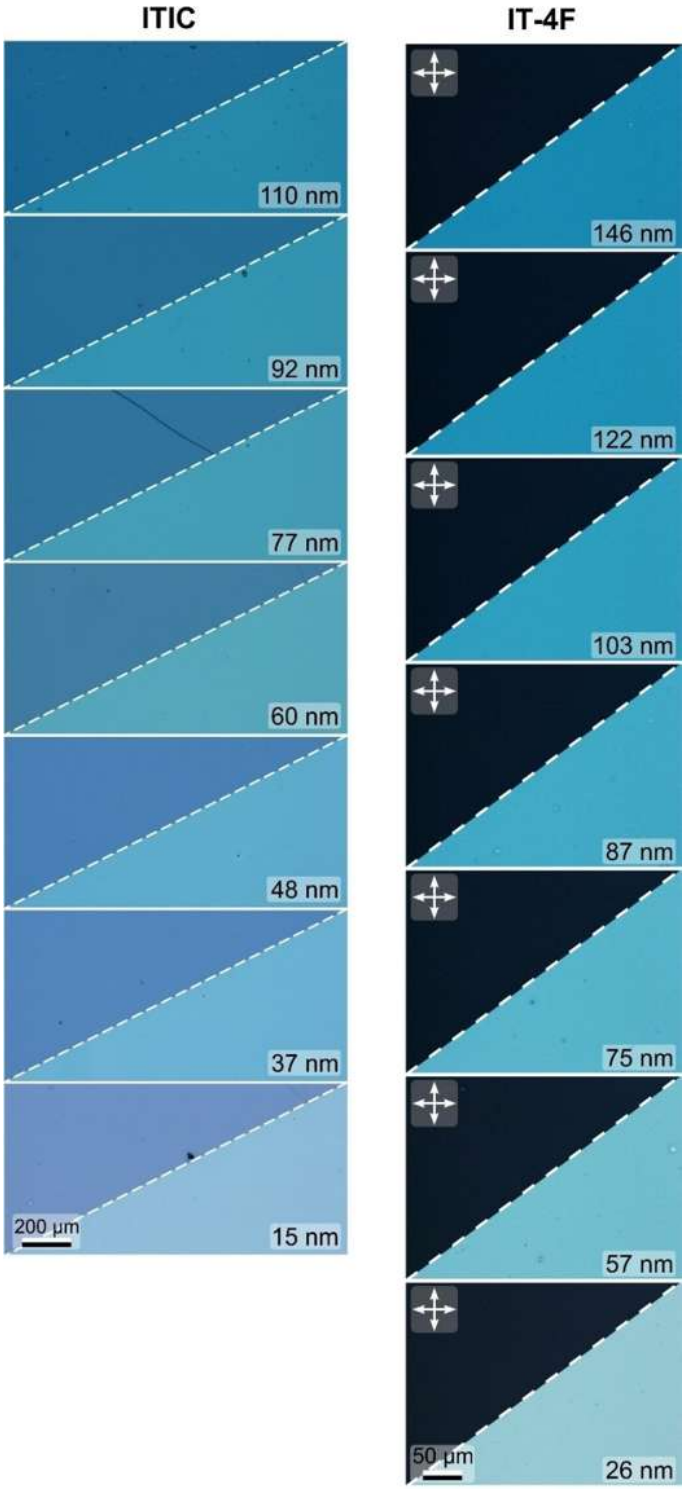

Figure S21. *Left*: Transmitted-light micrographs for ITIC thickness gradient laminated with PM6 recorded for ITIC thicknesses ranging from ~110 to ~20 nm (as indicated). For a given ITIC thickness, micrographs are shown for the bilayer (top-left panels) and ITIC only (bottom-right panels) regions. Note the comparable homogeneity for ITIC-only and bilayer regions, confirming that the lamination process does not damage or delaminate the ITIC films. *Right*: Optical micrographs for an as-deposited IT-4F thickness gradient sample recorded at film thicknesses ranging from 146 to 26 nm (as indicated). Both cross-polarized (top-left panels) and transmitted-light (bottom-right panels) micrographs are shown for a given thickness.

16. References

[1] L.A.A. Pettersson, L.S. Roman, O. Inganäs, *J. Appl. Phys.* **1999**, *86*, 487–496.

[2] P. Peumans, A. Yakimov, S.R. Forrest, *J. Appl. Phys.* **2003**, *93*, 3693–3723.

[3] D. Qin, P. Gu, R.S. Dhar, S.G. Razavipour, D. Ban, *Phys. Status Solidi Appl. Mater. Sci.* **2011**, *208*, 1967–1971.

[4] T. Stübinger, W. Brütting, *J. Appl. Phys.* **2001**, *90*, 3632–3641.

[5] J.J.M. Halls, K. Pichler, R.H. Friend, *J. Appl. Phys.* **1996**, *68*, 3120–3122.

[6] V. Bulović, S.R. Forrest, *Chem. Phys.* **1996**, *210*, 13–25.

[7] R.R. Lunt, N.C. Giebink, A.A. Belak, J.B. Benziger, S.R. Forrest, *J. Appl. Phys.* **2009**, *105*, 053711.

[8] K.J. Bergemann, S.R. Forrest, *Appl. Phys. Lett.* **2011**, *99*, 13–16.

[9] W.A. Luhman, R.J. Holmes, *Adv. Funct. Mater.* **2011**, *21*, 764–771.

[10] S.M. Menke, W.A. Luhman, R.J. Holmes, *Nat. Mater.* **2013**, *12*, 152–157.

[11] A.K. Topczak, T. Roller, B. Engels, W. Brütting, J. Pflaum, *Phys. Rev. B - Condens. Matter Mater. Phys.* **2014**, *89*, 201203.

[12] O. V Kozlov, Y.N. Luponosov, A.N. Solodukhin, B. Flament, *Org. Electron.* **2018**, *53*, 185–190.

[13] B.A.L. Raul, Y.N. Luponosov, W. Yang, N.M. Surin, O. Douhéret, J. Min, T.L.C. Jansen, S.A. Ponomarenko, M.S. Pshenichnikov, *Sci. Rep.* **2020**, *10*, 1–10.

[14] Y. Firdaus, V.M. Le Corre, S. Karuthedath, W. Liu, A. Markina, W. Huang, S. Chattopadhyay, M.M. Nahid, M.I. Nugraha, Y. Lin, A. Seitkhan, A. Basu, W. Zhang, I. McCulloch, H. Ade, J. Labram, F. Laquai, D. Andrienko, L.J.A. Koster, T.D. Anthopoulos, *Nat. Commun.* **2020**, *11*, 5220.

[15] M.T. Sajjad, A. Ruseckas, L.K. Jagadamma, Y. Zhang, I.D.W. Samuel, *J. Mater. Chem. A.* **2020**, *8*, 15687–15694.

[16] S. Chandrabose, K. Chen, A.J. Barker, J.J. Sutton, S.K.K. Prasad, J. Zhu, J. Zhou, K.C. Gordon, Z. Xie, X. Zhan, J.M. Hodgkiss, *J. Am. Chem. Soc.* **2019**, *141*, 6922–6929.

[17] L. Yu, D. Qian, S. Marina, F.A.A. Nugroho, A. Sharma, S. Hultmark, A.I. Hofmann, R. Kroon, J. Benduhn, D.M. Smilgies, K. Vandewal, M.R. Andersson, C. Langhammer, J. Martín, F. Gao, C. Müller, *ACS Appl. Mater. Interfaces*. **2019**, *11*, 21766−21774.

[18] S. Brixi, O.A. Melville, N.T. Boileau, B.H. Lessard, *J. Mater. Chem. C*. **2018**, *6*, 11972–11979.

[19] S. Marina, A.D. Scaccabarozzi, E. Gutierrez-Fernandez, E. Solano, A. Khirbat, L. Ciammaruchi, A. Iturrospe, A. Balzer, L. Yu, E. Gabirondo, X. Monnier, H. Sardon, T.D. Anthopoulos, M. Caironi, M. Campoy-Quiles, C. Müller, D. Cangialosi, N. Stingelin, J. Martin, *Adv. Funct. Mater.* **2021**, *31*, 2103784.

[20] S. Karuthedath, J. Gorenflot, Y. Firdaus, N. Chaturvedi, C.S.P. De Castro, G.T. Harrison, J.I. Khan, A. Markina, A.H. Balawi, T.A. Dela Peña, W. Liu, R.Z. Liang, A. Sharma, S.H.K. Paleti, W. Zhang, Y. Lin, E. Alarousu, D.H. Anjum, P.M. Beaujuge, S. De Wolf, I. McCulloch, T.D. Anthopoulos, D. Baran, D. Andrienko, F. Laquai, *Nat. Mater.* **2021**, *20*, 378–384.

[21] J. Schellenberg, *Syndiotactic Polystyrene: Synthesis, Characterization, Processing, and Applications*, John Wiley and Sons, **2009**.

[22] A. Perevedentsev, P.N. Stavrinou, P. Smith, D.D.C. Bradley, *J. Polym. Sci. Part B Polym. Phys.* **2015**, *53*, 1492–1506.

[23] A. Perevedentsev, M. Campoy-Quiles, *Nat. Commun.* **2020**, *11*, 3610.